INTERNATIONAL JOURNAL FOR NUMERICAL METHODS IN FLUIDS, VOL. 19, 493–512 (1994)

ENTRANCE FLOW IN ECCENTRIC ANNULAR DUCTS

K. VELUSAMY

Thermal Hydraulics Section, Indira Gandhi Centre for Atomic Research, Kalpakkam 603102, India

AND

VIJAY K. GARG

Internal Fluid Mechanics Division, NASA Lewis Research Center, Mail Stop 5-11, Cleveland, OH 44135, U.S.A.

SUMMARY

A control-volume-based solution of the complete set of Navier–Stokes equations for the laminar, three-dimensional developing flow in straight, eccentric, cylindrical annular ducts is described. Numerical results for velocity and pressure development, pressure defect and entrance lengths are presented for a wide range of duct parameters, i.e. relative eccentricity ε and radius ratio γ. The present results match very well with earlier numerical solutions for the limiting cases of developing flow in concentric ducts and fully developed flow in eccentric ducts. Comparison with earlier approximate results for developing flow in eccentric ducts indicates that the approximate model predicts the velocity and pressure development with an error of about 10%. However, the development length predicted by the approximate model is grossly in error. The pressure defect and development length in eccentric ducts are very high compared with their counterparts in concentric ducts. The pressure defect, development length and maximum velocity increase with the radius ratio for eccentric ducts, while the reverse is true for concentric ducts. Also, the apparent friction factor decreases as the eccentricity increases.

KEY WORDS Developing flow Eccentric annular ducts 3+D Navier–Stokes solution

1. INTRODUCTION

Eccentric annular ducts are occasionally used as fluid flow and heat transfer devices. The eccentricity may stem from design constraints or as a result of deformation in service from the nominally concentric configuration. The flow characteristics for an eccentric duct are far different from those for a concentric duct.[1] There is therefore a need for detailed analysis of the flow development in eccentric ducts.

Wilson[2] was perhaps the first to report a hydrodynamic entrance region solution for eccentric ducts. He solved a linearized version of the governing equations leading to a two-dimensional eigenvalue problem. However, the analytical expressions containing the solution were not evaluated.[3] Later Feldman *et al.*[3,4] reported a numerical solution for developing flow and temperature based on an approximate flow model. Their model assumes a relation between the cross-stream velocity components based on an idealization of the cross-stream flow. This idealization is not really valid in the presence of recirculation zones within the developing flow in an eccentric annulus. The effects of these recirculations on the main flow characteristics cannot be assessed by any simplified model. A complete solution of all three momentum equations along with the continuity equation is the only option. Also, Feldman *et al.*[3] provided a solution only for $\varepsilon > 0{\cdot}5$ and $\gamma > 0{\cdot}5$. The objective of this study is to provide a complete solution for

CCC 0271–2091/94/180493–20

Received December 1993
Revised March 1994

the problem of three-dimensional flow development in eccentric annular ducts for a wide range of duct parameters.

A literature survey indicates that no complete solution for flow development in eccentric annuli is available (see e.g. Reference 5 and similar earlier surveys). Recently Sathyamurthy *et al.*[6] and Choudhury and Karki[7] reported numerical results for mixed convection in eccentric annuli but for fully developed flows.

2. ANALYSIS

Consider an incompressible, Newtonian fluid entering a straight eccentric annulus. We assume negligible body forces and laminar flow with constant properties. In conformity with existing developing flow solutions in straight ducts, momentum diffusion in the axial direction is neglected in comparison with that in the cross-stream direction. This assumption renders the governing equations parabolic in the axial direction. We use bipolar co-ordinates (ξ, η, z) as shown in Figure 1. This co-ordinate system consists of an orthogonal family of circles in a plane, translated in the third (axial here) direction normal to the plane. The family of $\eta = \text{const.}$ circles is represented by

$$(x - a\coth\eta)^2 + y^2 = a^2\,\mathrm{cosech}^2\,\eta \quad \text{for } -\infty < \eta < \infty,$$

where a is the positive pole of the bipolar co-ordinate system located on the x-axis. The family of $\xi = \text{const.}$ circles is represented by

$$x^2 + (y - a\cot\xi)^2 = a^2\,\mathrm{cosec}^2\,\xi \quad \text{for } 0 \leqslant \xi \leqslant 2\pi.$$

The geometry of the eccentric annulus is characterized by two dimensionless parameters, the radius ratio $\gamma = r_i/r_o$, and the relative eccentricity $\varepsilon = e/(r_o - r_i)$.

The normalized equations for conservation of mass and momentum are[8]

$$\frac{1}{H^2}\frac{\partial}{\partial\xi}(HU) + \frac{1}{H^2}\frac{\partial}{\partial\eta}(HV) + \frac{\partial W}{\partial Z} = 0, \tag{1}$$

$$\frac{1}{H^2}\frac{\partial}{\partial\xi}(HU^2) + \frac{1}{H^2}\frac{\partial}{\partial\eta}(HUV) + \frac{\partial}{\partial Z}(UW) = \frac{1}{H^2}\left(\frac{\partial^2 U}{\partial\xi^2} + \frac{\partial^2 U}{\partial\eta^2}\right) - \frac{1}{H}\frac{\partial P'}{\partial\xi}$$
$$+ \frac{1}{H^2}\left[\frac{2}{H}\frac{\partial V}{\partial\xi}\frac{\partial H}{\partial\eta} - \frac{2}{H}\frac{\partial V}{\partial\eta}\frac{\partial H}{\partial\xi} - \frac{U}{H}\left(\frac{\partial^2 H}{\partial\xi^2} + \frac{\partial^2 H}{\partial\eta^2}\right)\right] + \frac{V}{H^2}\left(V\frac{\partial H}{\partial\xi} - U\frac{\partial H}{\partial\eta}\right), \tag{2a}$$

$$\frac{1}{H^2}\frac{\partial}{\partial\xi}(HUV) + \frac{1}{H^2}\frac{\partial}{\partial\eta}(HV^2) + \frac{\partial}{\partial Z}(VW) = \frac{1}{H^2}\left(\frac{\partial^2 V}{\partial\xi^2} + \frac{\partial^2 V}{\partial\eta^2}\right) - \frac{1}{H}\frac{\partial P'}{\partial\eta}$$
$$+ \frac{1}{H^2}\left[\frac{2}{H}\frac{\partial U}{\partial\eta}\frac{\partial H}{\partial\xi} - \frac{2}{H}\frac{\partial U}{\partial\xi}\frac{\partial H}{\partial\eta} - \frac{V}{H}\left(\frac{\partial^2 H}{\partial\xi^2} + \frac{\partial^2 H}{\partial\eta^2}\right)\right] + \frac{U}{H^2}\left(U\frac{\partial H}{\partial\eta} - V\frac{\partial H}{\partial\xi}\right), \tag{2b}$$

$$\frac{1}{H^2}\frac{\partial}{\partial\xi}(HUW) + \frac{1}{H^2}\frac{\partial}{\partial\eta}(HVW) + \frac{\partial}{\partial Z}(W^2) = \frac{1}{H^2}\left(\frac{\partial^2 W}{\partial\xi^2} + \frac{\partial^2 W}{\partial\eta^2}\right) - \frac{\mathrm{d}\bar{P}}{\mathrm{d}Z}. \tag{2c}$$

The integral form of the continuity equation at any duct cross-section is

$$\int_{\xi=0}^{\xi=\pi}\int_{\eta=\eta_o}^{\eta=\eta_i} WH^2\,\mathrm{d}\xi\,\mathrm{d}\eta = \frac{\pi}{8}\frac{1+\gamma}{1-\gamma}. \tag{3}$$

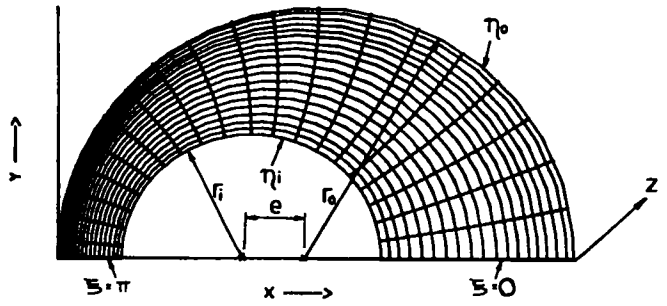

Figure 1. Bipolar co-ordinate system

In equations (2a)–(2c) the pressure field $P(\xi, \eta, Z)$ has been split into two parts such that

$$P(\xi, \eta, Z) = \bar{P}(Z) + P'(\xi, \eta).$$

This approximation has been used extensively for parabolic confined flows.

Owing to symmetry, only half the duct needs to be considered for the analysis. Hence the boundary conditions are

$$\begin{aligned} &U = \frac{\partial V}{\partial \xi} = \frac{\partial W}{\partial \xi} = 0 \quad \text{along } \xi = 0, \pi \quad \text{for } \eta_o \leqslant \eta \leqslant \eta_i \text{ and all } Z, \\ &U = V = W = 0 \qquad \text{along } \eta = \eta_i, \eta_o \quad \text{for } 0 \leqslant \xi \leqslant \pi \text{ and all } Z, \\ &U = V = \bar{P} = 0 \qquad \text{and} \quad W = 1 \quad \text{at } Z = 0 \quad \text{for all } \xi \text{ and } \eta. \end{aligned} \tag{4}$$

Equations (1)–(4) form a complete set of equations for the three components of velocity and two parts of pressure. The pressure defect K at any axial location is given by

$$K(Z) = 2\left[\left(\frac{dP}{dZ}\right)_f Z - \bar{P}(Z)\right],$$

where $(dP/dZ)_f$ is the pressure gradient for fully developed flow in the duct.

3. SOLUTION

The complete set of non-linear, interlinked partial differential equations is solved by the control-volume-based discretization method.[9] The discretization equations are given in Appendix I. The solution at any axial marching location is obtained in two stages. The first stage contains the solution for the axial velocity component and duct average pressure from equations (2c) and (3). The second stage contains the solution for the cross-stream velocity components and deviational pressure from equations (1), (2a) and (2b). At any axial marching location these two stages are repeated sufficiently to account for non-linearity and interlinkage of the equations. The procedure adopted for the solution is a modified form of Patankar and Spalding's method[10] for parabolic flows. The major modifications include (i) use of the SIMPLER algorithm[9] for resolving the cross-stream pressure–velocity coupling and (ii) use of Raithby and Schneider's

method[11] for evaluating the axial pressure gradient. During discretization of the governing equations the convection and diffusion fluxes are combined using the power law scheme.[9]

The discretization procedure yields a set of algebraic equations for each variable. The pentadiagonal system of algebraic equations for each variable is solved by a plane-by-plane method.[12,13] This method is an extension of the Thomas algorithm for the tridiagonal system of equations. Convergence at any marching step is assumed once the absolute sum of the residue R_ϕ corresponding to the variable ϕ in the discretization equation is less than δ, where

$$R_\phi = \sum_{i=1}^{n_\phi} |r_{i\phi}|.$$

The value of δ is taken to be 5×10^{-5} for the cross-stream equations and 10^{-5} for the axial momentum and integral continuity equations. No significant change in the results was observed when the value of δ for the cross-stream equations was reduced to 10^{-5}.

Results were first obtained on two grid patterns, one coarse and the other fine. For the coarse grid a non-uniform grid pattern of 13 × 15 (in the ξ- and η-direction respectively) was adopted in the cross-stream plane and results were obtained for the entire development length. For the fine grid a non-uniform grid pattern of 22 × 25 was adopted in the cross-stream plane and again results were obtained for the entire development length. The maximum difference in the maximum axial velocity, duct average pressure and pressure defect for the two grids was found to be less than 3%. However, the difference in the development length was about 10%. Hence the solution for the entire developing region was again obtained with a grid pattern of 28 × 38 for a particular case of $\varepsilon = \gamma = 0{\cdot}5$. The difference between the two fine grid solutions was found to be less than 1% in all quantities except in the development length for which it was about 3%. Thus the grid pattern of 22 × 25 was assessed to be satisfactory and was adopted for the results presented here. It may be pointed out that grids were packed near the duct walls where large velocity gradients exist.

In the axial direction very fine grids of size 10^{-7} were used near the duct inlet. As the flow developed, the step size was gradually increased. It was necessary to use a smaller axial step size for a higher eccentricity in order for the solution to converge within a prescribed number of iterations at every marching step. The maximum number of axial steps used was about 9360 for the case of $\varepsilon = \gamma = 0{\cdot}8$. The minimum number of axial steps was 175 for the case of $\varepsilon = 0{\cdot}001$ and $\gamma = 0{\cdot}4$. It was also found that refinement of the cross-stream grid leads to an increase in the number of axial steps required for solution.

Relaxation factors in the range 0·2–0·6 were used for solution. The number of iterations between the two stages of solution at each axial step was kept at six. However, reducing this to three produced only negligible change in the solution. The flow was taken to be fully developed once the maximum velocity W_{max} reached 99% of the fully developed value. Developing flow solutions were obtained for 10 different eccentric configurations covering a wide range of parameters, $\gamma = 0{\cdot}1$, 0·2, 0·5 and 0·8 and $\varepsilon = 0{\cdot}2$, 0·5, 0·8 and 0·9. Moreover, developing flow solutions for five concentric configurations ($\gamma = 0{\cdot}1$, 0·2, 0·4, 0·5 and 0·8) were obtained for the sake of comparison. The value of ε for a concentric configuration was taken as 0·001, since the co-ordinate transformation is singular for $\varepsilon = 0$.

4. ACCURACY

In order to validate the computer programme, the problem of fully developed flow in eccentric annuli was analysed first. The fully developed values of friction factor are compared against the

Table I. Values of 100% developed pressure gradient ($=2f\ Re$)

	ε				
γ	0·001	0·2	0·5	0·8	0·9
0·8	47·769 (47·960)	45·079 [45·262]	34·796 [34·960]	24·523 [24·608]	
0·5	47·460 (47·626)	44·968 [45·082]	35·193 [35·342]	25·493 [25·510]	
0·4	47·301 (47·356)				
0·2	46·096 (46·176)	44·138 [44·186]	36·365 [36·394]	28·441 [28·362]	
0·1	44·634 (44·686)				28·789 [28·560]

Key: ( ), analytical solution (Reference 1, p. 286); [ ], analytical solution of Tiedt reported in Reference 1, p. 326.

Table II. 100% developed W_{max}

	ε				
γ	0·001	0·2	0·5	0·8	0·9
0·8	1·5003 (1·501)	2·029	2·430	2·453	
0·5	1·5055 (1·508)	2·011	2·372 [2·373]	2·350	
0·4	1·5144 (1·513) [1·516]				
0·2	1·5383 (1·537)	1·956	2·218	2·183	
0·1	1·5689 (1·567)				2·075 [2·152] [2.076]*

Key: ( ), analytical solution (Reference 1, p. 286); [ ], solution of Feldman *et al.*[3]; [ ]*, solution of Feldman *et al.*[3] with fine grid.

analytical results of Tiedt (reported in Reference 1) in Table I. Clearly the maximum difference is only 0·8%. This comparison also justifies the adequacy of the grid size in the cross-stream plane. Next the problem of flow development in concentric annular ducts was solved and compared with the results available in the literature, as shown in Tables I and II. It is clear that the present results match the analytical results almost exactly. The maximum difference in friction factor is 0·4% and that in W_{max} is less than 0·2%. Shown in Table III are the present values of development length in concentric ($\varepsilon = 0{\cdot}001$) annuli compared against the numerical values of Roy[14] for various values of γ. It may be noted that for all values of γ except $\gamma = 0{\cdot}2$ the present results match those of Roy very well, the maximum difference being 3·5%. For $\gamma = 0{\cdot}2$, however,

Table III. Development length

	ε				
γ	0·001	0·2	0·5	0·8	0·9
0·8	0·01196 (0·0113)	0·1310	0·2064	0·2659	
0·5	0·01226 (0·0121)	0·1177	0·1478 [0·254]	0·0978	
0·4	0·0124 (0·0128)				
0·2	0·0148 (0·0158)	0·0905	0·0886	0·0835	
0·1	0·0183 (0·0180)				0·072 [0·106]

Key: ( ), solution of Roy[14] reported in (Reference 1, p. 288); [ ], solution of Feldman *et al.*[3].

Table IV. Pressure defect at 99% flow development

	ε				
γ	0·001	0·2	0·5	0·8	0·9
0·8	0·6582 (0·650)	1·0782	2·0424	2·1824	
0·5	0·6694 (0.688)*	1·0544	1·928 [2·144]	1·9382	
0·4	0·694 (0·672) [0·714]				
0·2	0·7164 (0·714)	0·9976	1·6031	1·591	
0·1	0·777 (0·766) (0·784)*				1·4256 [1·571]

Key: ( ), solution of Sparrow and Lin[15] reported in (Reference 1, p. 288); ( )*, solution of Liu[16] reported in Reference 1, p. 288; [ ], solution of Feldman *et al.*[3].

the difference is about 6%. Shown in Table IV are the present results for pressure defect compared against similar results of Sparrow and Lin[15] and Liu[16] for concentric annuli. The present results deviate from those of References 15 and 16 by about 3%. The present results for the development of axial velocity in a concentric annulus of radius ratio 0·1 are compared with the numerical values of Sparrow and Lin[15] in Figure 2. Clearly the comparison is very good in the entire development region.

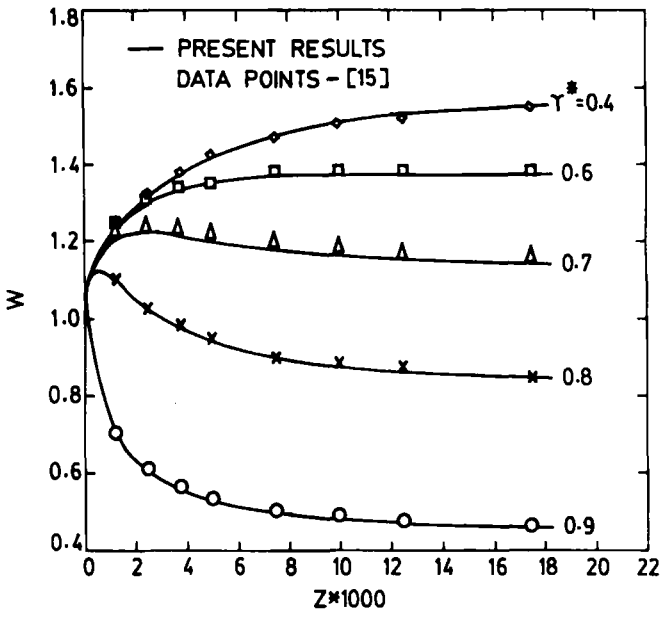

Figure 2. Development of axial velocity ($\gamma = 0{\cdot}1$, $\varepsilon = 0{\cdot}001$)

5. RESULTS AND DISCUSSION

The developing flow results are presented in the following form:

(i) development of maximum axial velocity component W_{max} along the flow (axial) direction
(ii) development of duct average pressure and pressure defect along the axial direction
(iii) iso-axial-velocity-component contours at various cross-sections of the duct along the flow direction
(iv) cross-stream flow field at various duct cross-sections.

5.1. Development of W_{max}

The developing W_{max} is shown in Figures 3(a) and 3(b) for various values of eccentricity ε and radius ratio γ. The maximum velocity increases continuously as fluid is ejected out of the boundary layers developing near the duct walls. The increase is also due to ejection of fluid from the narrow portion of the duct towards the wider portion. The value of W_{max} is considerably higher for eccentric ducts than for concentric ducts and this is true for all values of the radius ratio. It is due to the non-uniformity associated with eccentric annuli and the resulting confinement of the fluid within a relatively smaller cross-section.

The fully developed values of W_{max} are given in Table II for various values of ε and γ. For a high radius ratio such as $\gamma = 0{\cdot}8$, W_{max} increases continuously with ε. However, for smaller values of γ such as 0·5 and 0·2, W_{max} displays a maximum at about $\varepsilon = 0{\cdot}5$. For concentric ducts ($\varepsilon = 0{\cdot}001$) it can be seen from Table II that W_{max} decreases slightly as the radius ratio increases. However, for eccentric ducts W_{max} increases with the radius ratio for any value of ε. Also, this increase is higher for higher values of ε.

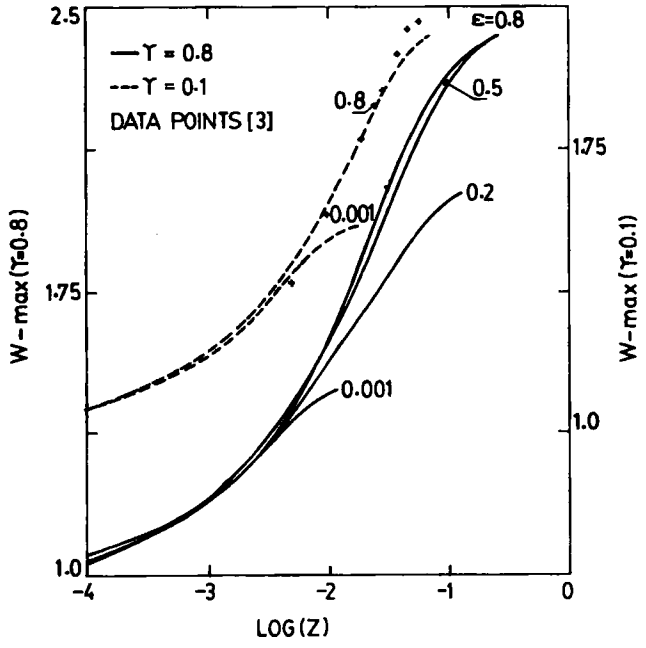

Figure 3(a). Development of axial velocity ($\gamma = 0{\cdot}1$ and $0{\cdot}8$)

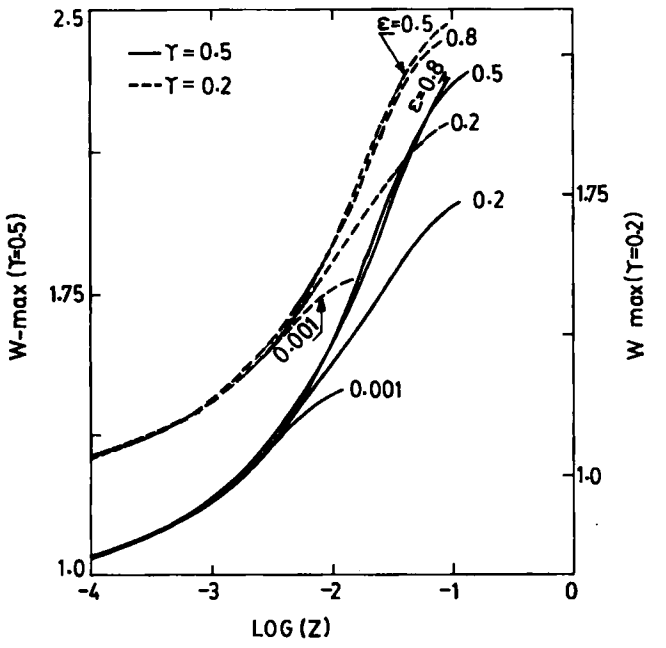

Figure 3(b). Development of axial velocity ($\gamma = 0{\cdot}2$ and $0{\cdot}5$)

The value of W_{max} predicted by Feldman *et al.*[3] for $\varepsilon = 0{\cdot}9$ and $\gamma = 0{\cdot}1$ using the simplified model is also shown in Figure 3(a). It can be observed that the simplified model underpredicts W_{max} at small Z-values and overpredicts it at large Z-values. One of the reasons for this overprediction is the uniform grid size employed in the ξ-direction by Feldman *et al.* As the eccentricity increases, the bipolar co-ordinate system concentrates grids in the narrow part of the annulus with sparser grids in the wider part of the annulus. The fully developed W_{max} predicted by Feldman *et al.* for $\varepsilon = 0{\cdot}9$ and $\gamma = 0{\cdot}1$ is 2·152 with a grid pattern of 24 × 32 and 2·076 with a grid pattern of 48 × 32. The present value of W_{max} is 2·075 with a grid pattern of only 21 × 21 owing to the use of a non-uniform grid that is dense near the walls and coarse away from the walls.

5.2. *Development of axial duct pressure*

The development of duct average pressure $\bar{P}(Z)$ is shown in Figures 4(a) and 4(b). It may be mentioned that $\bar{P}(Z) = 2f_{app}Re\,Z$. Clearly $\bar{P}(Z)$ is a strong function of ε but only a weak function of γ. For a substantial part of the entrance length the value of $f_{app}Re$ decreases with an increase in ε. This is due to the fact that as ε increases, the effective participation of the duct walls (especially the inner wall) in shearing the fluid decreases. In Figures 4(a) and 4(b) the development curves corresponding to concentric ducts ($\varepsilon = 0{\cdot}001$) are of shorter length and coincide with those for $\varepsilon = 0{\cdot}2$. Also, in a small region close to the duct inlet the value of $f_{app}Re$ for an eccentric duct is nearly the same as that for a concentric duct.

5.3. *Development of pressure defect*

The developing pressure defect K for various values of ε and γ is shown in Figures 5(a) and 5(b). It can be observed that in the developing region K increases with ε for all values of γ. Also, the pressure defect for an eccentric duct is relatively larger than that for a concentric duct. The numerical value of K at 99% of flow development is shown in Table IV. From this table it is clear that for concentric ducts the pressure defect decreases with an increase in γ. However, for eccentric ducts the reverse is true. Also, for a fixed radius ratio the increase in K with ε is considerable only up to $\varepsilon = 0{\cdot}5$, while for $\varepsilon > 0{\cdot}5$ the change in K is small. Comparing with concentric ducts, the pressure defect is considerably high, as much as 50% more for mildly eccentric ducts ($\varepsilon = 0{\cdot}2$) and as much as 200% more for highly eccentric ducts ($\varepsilon > 0{\cdot}5$). One of the reasons for such high values of K in eccentric ducts is the energy required to support the circumferential flow (ejected from the narrow part of the annulus to the wider part) and its associated recirculation in the duct. These are absent in a concentric duct. Moreover, for a fixed radius ratio the total momentum of the fluid entering the duct is the same for both concentric and eccentric ducts. When the flow attains full development, however, the velocity profile in an eccentric duct is more non-uniform than that in a concentric duct. Thus the total momentum of the fluid at full development is higher in an eccentric duct than in a concentric duct. This disparity in momentum is the other reason for higher values of K in eccentric ducts.

The developing pressure defect predicted by Feldman *et al.*[3] for two eccentric duct configurations, namely $\varepsilon = \gamma = 0{\cdot}5$ and $\varepsilon = 0{\cdot}9$ and $\gamma = 0{\cdot}1$, is also shown in Figures 5(b) and 5(a). It is clear that the results of Feldman *et al.* compare reasonably well with the present results in the region close to the inlet. However, away from the inlet Feldman's approximate model overpredicts K by about 10%.

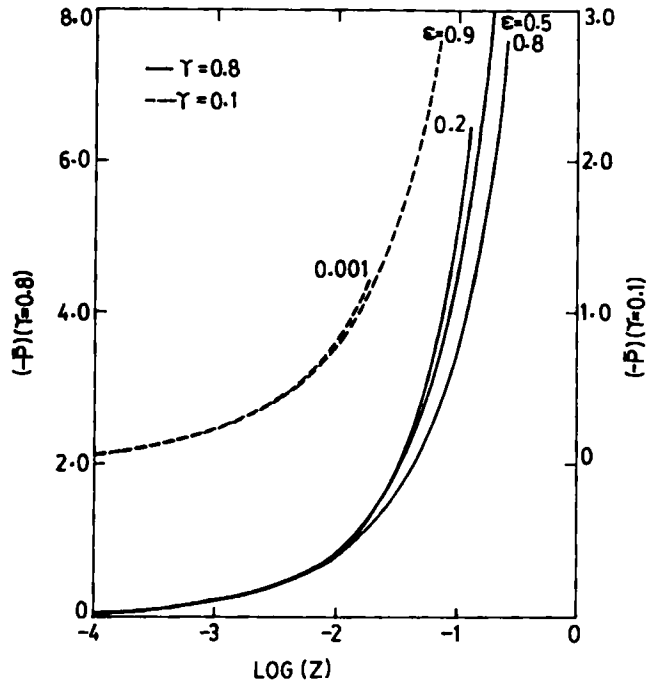

Figure 4(a). Development of $\bar{P}(\gamma = 0{\cdot}1$ and $0{\cdot}8)$

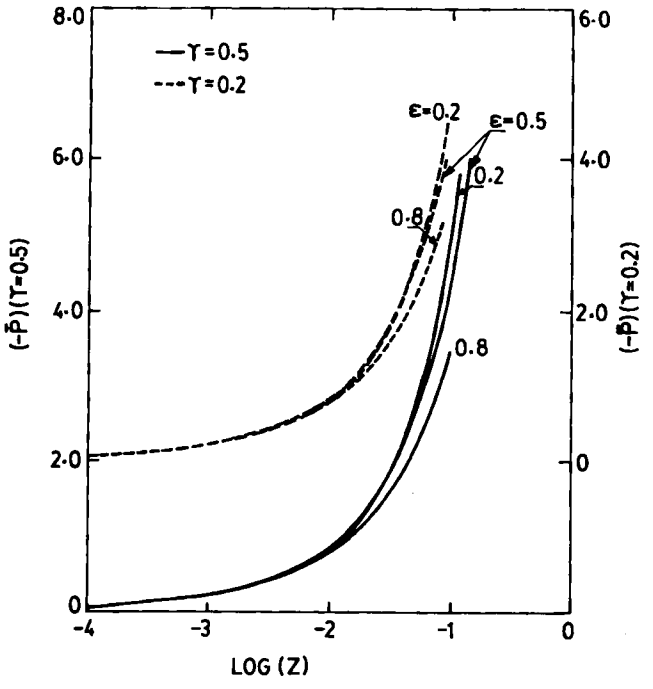

Figure 4(b). Development of $\bar{P}(\gamma = 0{\cdot}2$ and $0{\cdot}5)$

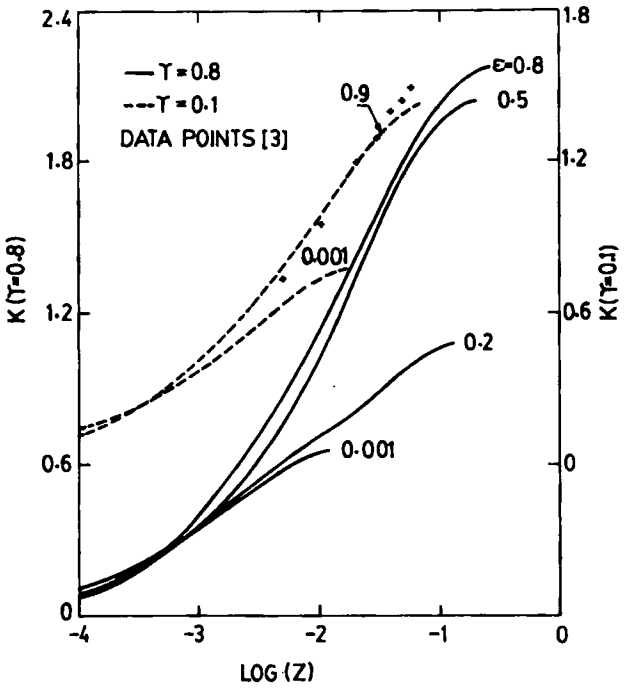

Figure 5(a). Development of pressure defect (γ = 0·1 and 0·8)

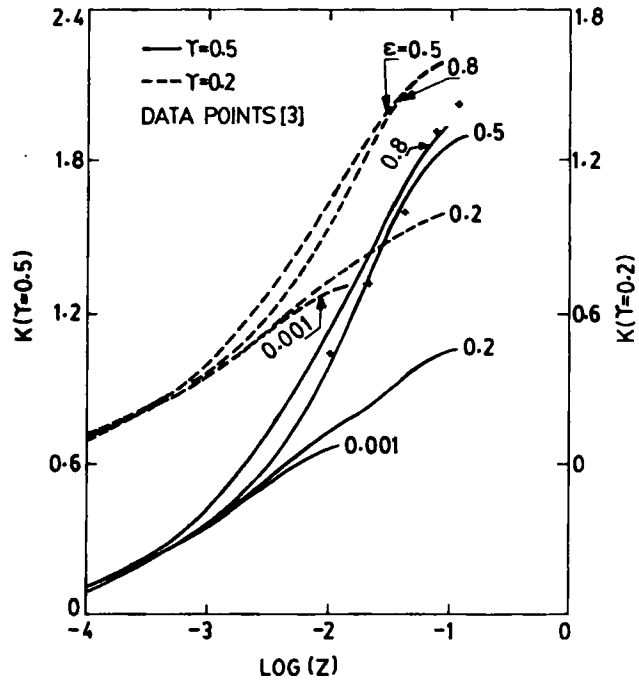

Figure 5(b). Development of pressure defect (γ = 0·2 and 0·5)

5.4. *Entrance length*

The flow development lengths in concentric and eccentric ducts are given in Table III for various values of ε and γ. Clearly the flow development length in an eccentric duct is very high compared with that in a concentric duct. For example, the ratio of development length in an eccentric duct to that in a concentric duct is about 22 for $\varepsilon = \gamma = 0{\cdot}8$ and about six for $\varepsilon = \gamma = 0{\cdot}2$. The reason for this increased flow development length in eccentric ducts is the length required to transport fluid from the narrow part to the wider part of the annulus. This is absent in a concentric duct. Another interesting feature is that for the parameters studied, the development length is maximum when $\varepsilon = \gamma$.

It is clear from Table III that the development length in the case of concentric ducts decreases with an increase in radius ratio. However, the reverse is true in the case of eccentric ducts for all values of eccentricity. The flow development lengths predicted by Feldman *et al.*[3] for two duct configurations are also given in Table III. Clearly the approximate model of Feldman *et al.* overpredicts the flow development length considerably.

5.5. *Development of axial velocity component*

The iso-axial-velocity-component contours at different axial locations are shown in Figures 6(a)–6(c) for some selected eccentric duct configurations. It is seen that at the smallest value of $Z(\approx 0{\cdot}0015)$ the potential core region (engulfed by the $W = 1{\cdot}2$ contour) is large and the viscous boundary layer region (between the $W = 1{\cdot}2$ contour and the duct walls) is small. As the flow

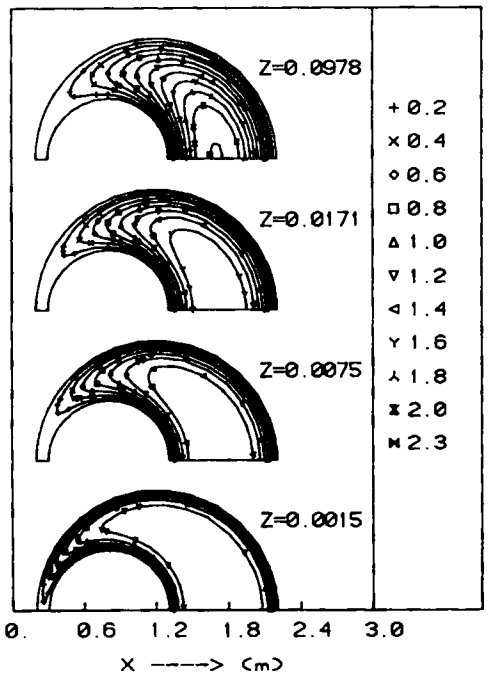

Figure 6(a). Iso-axial-velocity contours ($\gamma = 0{\cdot}5$, $\varepsilon = 0{\cdot}8$)

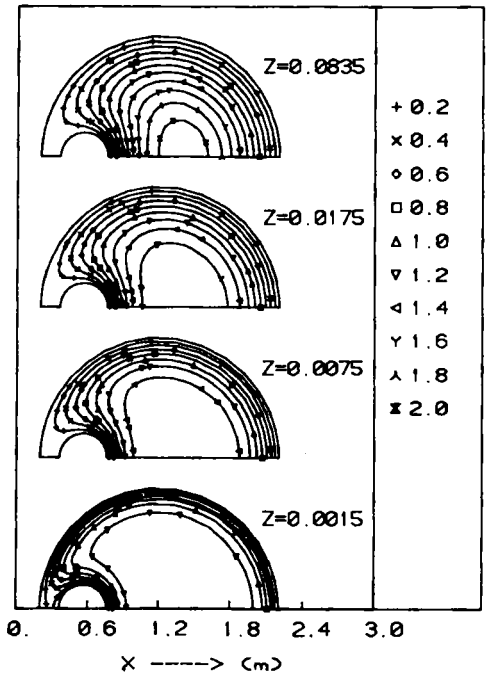

Figure 6(b). Iso-axial-velocity contours ($\gamma = 0{\cdot}2$, $\varepsilon = 0{\cdot}8$)

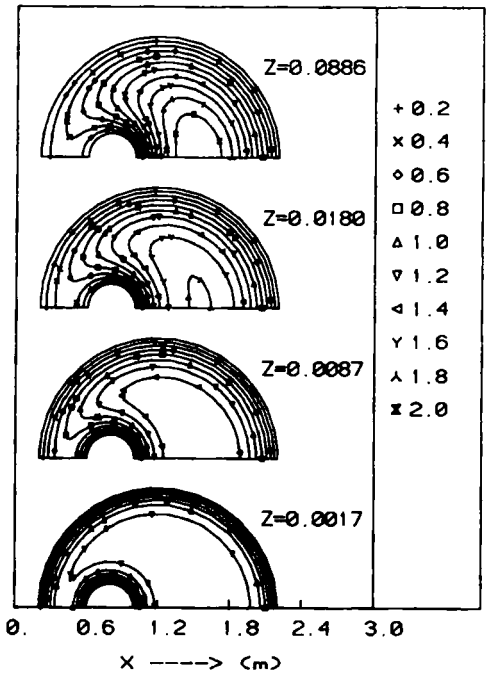

Figure 6(c). Iso-axial-velocity contours ($\gamma = 0{\cdot}2$, $\varepsilon = 0{\cdot}5$)

develops, the potential core region shrinks and moves towards the wider part of the annulus, while the boundary layer region increases. Also, as the flow develops, the velocity in the core increases owing to the efflux of fluid from the developing boundary layers and from the narrow part of the annulus. In Figures 6(a)–6(c) the largest value of Z corresponds to the 99% developed condition.

At small values of Z the contours are packed near the duct walls (especially in the narrow part of the annulus) and become increasingly sparse as the flow develops. This indicates high shear near the inlet. Also, for a fixed value of γ, the higher the eccentricity, the smaller is the value of W in the narrow part of the annulus.

5.6. *Cross-stream flow field*

The cross-stream flow field at different axial locations is shown in Figures 7(a)–7(c) for some eccentric ducts. In these figures the length of the arrows is proportional to the magnitude of the cross-stream velocity except for arrows marked with an $\times$. The scale of this vector plot is shown at the top of the figures. These figures show clearly that the fluid ejected out of the narrow part of the annulus flows transversely towards the wider part. Also, fluid is ejected out of the boundary layers developing over the duct walls. The strength of the cross-stream flow reduces as the main flow develops, as indicated by smaller-sized arrows.

Referring to Figures 7(a) and 7(b) representing highly eccentric ducts, the transverse flow is quite similar to cross-flow over a cylinder represented here by the inner tube. The transverse flow originating in the narrow part of the annulus near the duct inlet (lowest Z-value) separates from the inner tube at some point and induces a recirculation. The same transverse flow creates another recirculation near the outer wall as well. These recirculations persist even in planes far

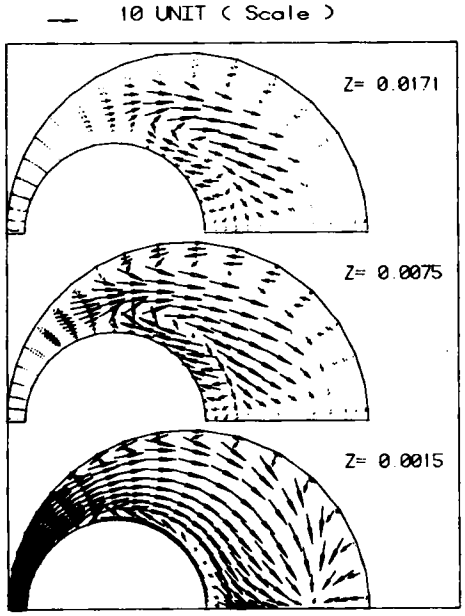

Figure 7(a). Cross-stream flow field ($\gamma = 0{\cdot}5$, $\varepsilon = 0{\cdot}8$)

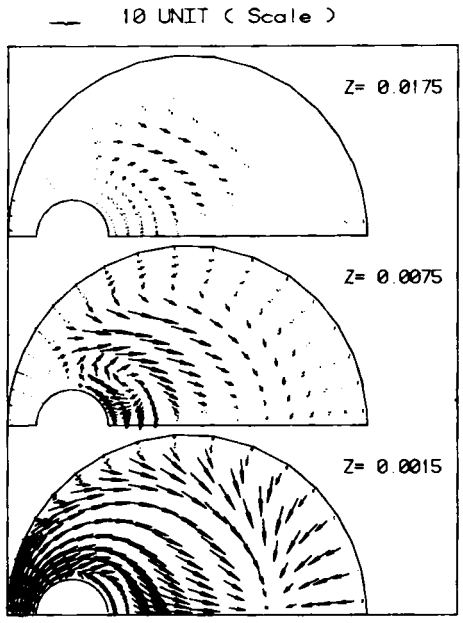

Figure 7(b). Cross-stream flow field ($\gamma = 0{\cdot}2$, $\varepsilon = 0{\cdot}8$)

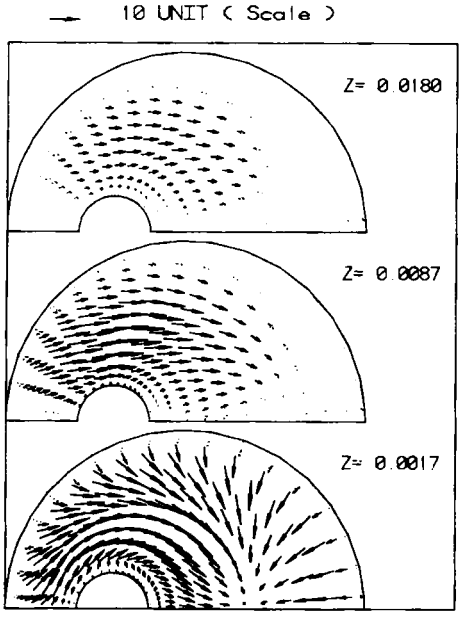

Figure 7(c). Cross-stream flow field ($\gamma = 0{\cdot}2$, $\varepsilon = 0{\cdot}5$)

away from the duct inlet. Clearly these recirculations depend on the eccentricity as well as the radius ratio. From Figures 7(a) and 7(b) it is clear that for a fixed ε, the larger the value of γ, the wider are the zones of recirculations and the longer is the axial length over which recirculations persist.

Referring to Figure 7(c) corresponding to $\varepsilon = 0{\cdot}5$ and $\gamma = 0{\cdot}2$, it is clear that there is no recirculation near the outer tube. However, there is a recirculation near the inner tube but its extent is very small. Comparing Figures 7(b) and 7(c), we find that for a fixed radius ratio the extent of recirculation increases with the eccentricity. The approximate model of Feldman *et al.*[3] cannot support these recirculations. Even in the absence of recirculation, Feldman's model is only approximate in estimating the actual cross-stream flow. However, the values of pressure defect predicted by Feldman *et al.*[3] for two geometries, namely $\varepsilon = \gamma = 0{\cdot}5$ and $\varepsilon = 0{\cdot}9$ and $\gamma = 0{\cdot}1$, do not differ much from the present results. One of the reasons for this fortunate comparison is that for these two cases there is no recirculation beyond $Z \approx 0{\cdot}002$ and even at locations $Z < 0{\cdot}002$ the recirculation zone is very small. The absence of recirculation is because of relatively small eccentricity in the case of $\varepsilon = \gamma = 0{\cdot}5$ and very small radius ratio in the case of $\varepsilon = 0{\cdot}9$ and $\gamma = 0{\cdot}1$. Whereas the approximate model of Feldman *et al.*[3] can predict K well for geometries with no recirculation zones, it cannot predict the development length correctly for any geometric configuration.

6. CONCLUSIONS

The problem of laminar, three-dimensional flow development in the entrance region of eccentric cylindrical annuli has been solved using the complete set of Navier–Stokes equations. Results have been obtained for a wide range of duct parameters. By comparing the present solution with an earlier approximate model, the validity and degree of approximation in the earlier model are assessed. Also, the flow development parameters in eccentric and concentric ducts are compared. The following conclusions are drawn based on this analysis.

(i) The maximum axial velocity in eccentric ducts is high compared with that in concentric ducts. W_{max} increases with the radius ratio in an eccentric duct but decreases in a concentric duct.

(ii) The product $f_{app}Re$ is a strong function of eccentricity but a weak function of radius ratio. It decreases as the eccentricity increases.

(iii) The total pressure defect in an eccentric duct is very high compared with that in a concentric duct. This is due to a gain in the momentum of the fluid and to cross-stream recirculations associated with eccentric ducts. The pressure defect increases with the radius ratio in an eccentric duct but decreases in a concentric duct. The approximate model of Feldman *et al.*[3] overpredicts the pressure defect by about 10%.

(iv) The flow development length in eccentric ducts is very high compared with that in concentric ducts. In eccentric ducts the development length increases with the radius ratio, while the opposite is true for concentric ducts. The approximate model of Feldman *et al.*[3] overpredicts the development length considerably.

(v) The transverse flow from the narrow part of the annulus to the wider part induces recirculations around the inner and outer walls of the annulus. The extent of these recirculating zones increases with eccentricity and radius ratio.

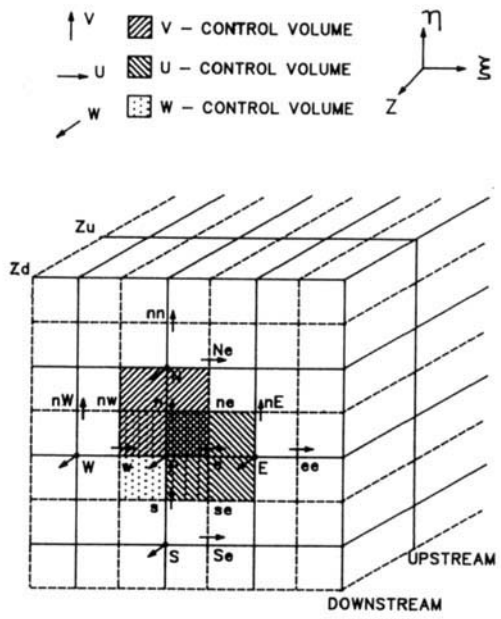

Figure 8. Staggered grid lay-out

APPENDIX I

The discretization equations are derived by integrating the governing partial differential equations over their respective control volumes. The control volumes corresponding to the cross-stream velocity components U and V are staggered in their respective directions ξ and η as shown in Figure 8.

Integration of the ξ-momentum equation (2a) over the control volume surrounding point 'e' in Figure 8, i.e. over the control volume extending from ξ_P to ξ_E, from η_{se} to η_{ne}, and from Z_u to Z_d (where subscripts 'u' and 'd' denote upstream and downstream locations respectively), yields

$$(J_E - J_P) + (J_{ne} - J_{se}) + (J_{de} - J_{ue}) = (P'_P - P'_E)\bar{H}\Delta\eta\Delta Z + \overline{S}_\xi, \tag{5}$$

where the fluxes J are given by

$$J_E = \left(HU^2 - \frac{\partial U}{\partial \xi}\right)_E \Delta\eta\Delta Z, \qquad J_P = \left(HU^2 - \frac{\partial U}{\partial \xi}\right)_P \Delta\eta\Delta Z,$$

$$J_{ne} = \left(HVU - \frac{\partial U}{\partial \eta}\right)_{ne} \Delta\xi\Delta Z, \qquad J_{se} = \left(HVU - \frac{\partial U}{\partial \eta}\right)_{se} \Delta\xi\Delta Z,$$

$$J_{de} = (WU)_{de}\overline{H^2}\Delta\xi\Delta\eta, \qquad J_{ue} = (WU)_{ue}\overline{H^2}\Delta\xi\Delta\eta$$

and the source term $\overline{S_\xi}$ is given later. Integration of the continuity equation (1) over the same control volume, multiplication by U_e, and subtraction from equation (5) yields

$$(J_E - F_E U_e) - (J_P - F_P U_e) + (J_{ne} - F_{ne} U_e) - (J_{se} - F_{se} U_e) + (J_{de} - F_{de} U_e) - (J_{ue} - F_{ue} U_e) = (P'_P - P'_E)\bar{H}\Delta\eta\Delta Z + \overline{S_\xi}, \quad (6)$$

where the Fs are defined later. From the generalized formulation for combining the convective and diffusive fluxes (Reference 9, p. 99), equation (6) reduces to

$$a_e U_e = a_{ee} U_{ee} + a_w U_w + a_{Ne} U_{Ne} + a_{Se} U_{Se} + a_{ue} U_{ue} + (P'_P - P'_E)\bar{H}\Delta\eta\Delta Z + \overline{S_\xi}, \quad (7)$$

where

$$a_{ee} = D_E A(|P_E|) + [\![-F_E, 0]\!], \qquad F_E = (HU)_E \Delta\eta\Delta Z, \qquad D_E = \frac{\Delta\eta\Delta Z}{\Delta\xi}, \qquad P_E = \frac{F_E}{D_E},$$

$$a_w = D_P A(|P_P|) + [\![F_P, 0]\!], \qquad F_P = (HU)_P \Delta\eta\Delta Z, \qquad D_P = \frac{\Delta\eta\Delta Z}{\Delta\xi}, \qquad P_P = \frac{F_P}{D_P},$$

$$a_{Ne} = D_{ne} A(|P_{ne}|) + [\![-F_{ne}, 0]\!], \qquad F_{ne} = (HV)_{ne} \Delta\xi\Delta Z, \qquad D_{ne} = \frac{\Delta\xi\Delta Z}{\Delta\eta}, \qquad P_{ne} = \frac{F_{ne}}{D_{ne}},$$

$$a_{Se} = D_{se} A(|P_{se}|) + [\![F_{se}, 0]\!], \qquad F_{se} = (HV)_{se} \Delta\xi\Delta Z, \qquad D_{se} = \frac{\Delta\xi\Delta Z}{\Delta\eta}, \qquad P_{se} = \frac{F_{se}}{D_{se}},$$

$$a_{ue} = W_{ue}\overline{H}^2 \Delta\xi\Delta\eta, \qquad a_e = a_{ee} + a_w + a_{Ne} + a_{Se} + a_{ue},$$

$$\overline{S_\xi} = \left(\overline{\frac{2}{H}\frac{\partial H}{\partial \eta}}\right)(V_E - V_P)\Delta\eta\Delta Z - \left(\overline{\frac{2}{H}\frac{\partial H}{\partial \xi}}\right)(V_{ne} - V_{se})\Delta\xi\Delta Z + \Delta\xi\Delta\eta\Delta Z\left\{\left(\overline{\frac{\partial H}{\partial \xi}}\right)\overline{V}_e^2 - \left(\overline{\frac{\partial H}{\partial \eta}}\right)(\overline{UV})_e - U_e\left[\overline{\frac{1}{H}\left(\frac{\partial^2 H}{\partial \xi^2} + \frac{\partial^2 H}{\partial \eta^2}\right)}\right]\right\}$$

and the symbol $[\![\ ]\!]$ indicates the maximum of the values contained. The definition of the function $A(|P|)$ depends upon the scheme used.[9] For example, for the upwind scheme $A(|P|) = 1$, while for the power law scheme, $A(|P|) = [\![0, (1 - 0{\cdot}1|P|)^5]\!]$.

Similarly, the discretization equation for η-momentum can be derived by integrating equation (2b) over the control volume surrounding point 'n' in Figure 8 to yield

$$a_n V_n = a_{nE} V_{nE} + a_{nW} V_{nW} + a_{nn} V_{nn} + a_s V_s + a_{un} V_{un} + (P'_P - P'_N)\bar{H}\Delta\xi\Delta Z + \overline{S_\eta}, \quad (8)$$

where the coefficients a are similar to those in equation (7) and

$$\overline{S_\eta} = \left(\overline{\frac{2}{H}\frac{\partial H}{\partial \xi}}\right)(U_N - U_P)\Delta\xi\Delta Z - \left(\overline{\frac{2}{H}\frac{\partial H}{\partial \eta}}\right)(U_{ne} - U_{nw})\Delta\eta\Delta Z + \Delta\xi\Delta\eta\Delta Z\left\{\left(\overline{\frac{\partial H}{\partial \eta}}\right)\overline{U}_n^2 - \left(\overline{\frac{\partial H}{\partial \xi}}\right)(\overline{UV})_n - V_n\left[\overline{\frac{1}{H}\left(\frac{\partial^2 H}{\partial \xi^2} + \frac{\partial^2 H}{\partial \eta^2}\right)}\right]\right\}.$$

A similar integration performed on equation (2c) over the control volume surrounding point 'P' in Figure 8 yields

$$a_P W_P = a_E W_E + a_W W_W + a_N W_N + a_S W_S + a_u W_{uP} + \overline{S_Z}, \tag{9}$$

where the coefficients a are similar to those in equation (7) and

$$\overline{S_Z} = -\frac{\partial \bar{P}}{\partial Z}\,\overline{H^2}\Delta\xi\Delta\eta\Delta Z.$$

The continuity equation (1), upon integration over the control volume surrounding point 'P' in Figure 8, yields

$$[(HU)_e - (HU)_w]\Delta\eta\Delta Z + [(HV)_n - (HV)_s]\Delta\xi\Delta Z = -(W_P - W_{uP})\overline{H^2}\Delta\xi\Delta\eta. \tag{10}$$

It may be noted that a fully implicit procedure is adopted in the parabolic Z-direction. Hence in equations (7)–(9) the unknowns without the subscript 'u' correspond to the downstream Z-plane and those with the subscript 'u' correspond to the upstream Z-plane.

APPENDIX II: NOMENCLATURE

a	location of positive pole of bipolar co-ordinate system
D_h	hydraulic diameter, $2(r_0 - r_i)$
e	distance between centres of inner and outer cylinders
f	Fanning friction factor for fully developed flow, $(d\bar{p}/dz)D_h/2\rho w_e^2$
f_{app}	apparent Fanning friction factor in flow development region, $[(\bar{p}(z) - \bar{p}(0))/z]D_h/2\rho w_e^2$
H	dimensionless scale factor, $(a/D_h)/(\cosh\eta - \cos\xi)$
K	pressure defect
n_ϕ	number of control volumes in cross-section for variable ϕ
p	total dimensional pressure (function of (ξ, η, z))
P	total dimensionless pressure, $p/(\rho w_e^2)$
$\bar{p}$	dimensional duct pressure averaged over cross-section
$\bar{P}$	dimensionless duct pressure averaged over cross-section, $\bar{p}/\rho w_e^2$
p'	dimensional deviational pressure (function of (ξ, η))
P'	dimensionless deviational pressure, $p' D_h^2/\rho\nu^2$
$r_{i\phi}$	residue of discretized equation for ith control volume for variable ϕ
r_i	radius of inner cylinder
r_o	radius of outer cylinder
r^*	$(r - r_i)/(r_o - r_i)$ in Figure 2
Re	Reynolds number, $w_e D_h/\nu$
R_ϕ	absolute sum of $r_{i\phi}$ taken over n_ϕ
u	velocity component in ξ-direction
U	dimensionless counterpart of u, uD_h/ν
v	velocity component in η-direction
V	dimensionless counterpart of v, vD_h/ν
w	velocity component in z-direction
w_e	uniform axial velocity at entrance
W	dimensionless counterpart of w, w/w_e
W_{max}	maximum value of W at any duct cross-section

x cross-stream Cartesian co-ordinate (Figure 1)
y cross-stream Cartesian co-ordinate (Figure 1)
z axial co-ordinate normal to x–y plane
Z dimensionless axial co-ordinate, $z/D_h Re$

Greek letters

δ small number for checking convergence
ε relative eccentricity, $e/(r_o - r_i)$
γ radius ratio of duct, r_i/r_o
η bipolar co-ordinate (Figure 1)
η_i value of η on inner cylinder, $\cosh^{-1}\{[\gamma(1+\varepsilon^2)+(1-\varepsilon^2)]/2\varepsilon\gamma\}$
η_o value of η on outer cylinder, $\cosh^{-1}\{[\gamma(1-\varepsilon^2)+(1+\varepsilon^2)]/2\varepsilon\}$
ν kinematic viscosity of fluid
ρ density of fluid
ξ bipolar co-ordinate (Figure 1)

REFERENCES

1. R. K. Shah and A. L. London, *Laminar Flow Forced Convection in Ducts*, Academic, New York, 1978.
2. J. T. Wilson, 'Analysis of fluid flow in the entrance region of a duct with an eccentric annular cross section', *Ph.D. Thesis*, University of Houston, 1974.
3. E. E. Feldman, R. W. Hornbeck and J. F. Osterle, 'A numerical solution of laminar developing flow in eccentric annular ducts', *Int. J. Heat Mass Transfer*, **25**, 231–241 (1982).
4. E. E. Feldman, R. W. Hornbeck and J. F. Osterle, 'A numerical solution of developing temperature for laminar developing flow in eccentric annular ducts', *Int. J. Heat Mass Transfer*, **25**, 243–253 (1982).
5. E. R. G. Eckert *et al.*, 'Heat transfer—a review of 1991 literature', *Int. J. Heat Mass Transfer*, **35**, 3153–3235 (1992).
6. P. Sathyamurthy, K. C. Karki and S. V. Patankar, 'Laminar, fully developed mixed convection in a vertical eccentric annulus', *Numer. Heat Transfer A*, **22**, 71–85 (1992).
7. D. Choudhury and K. C. Karki, 'Laminar mixed convection in a horizontal eccentric annulus', *Numer. Heat Transfer A*, **22**, 87–108 (1992).
8. W. F. Hughes and E. W. Gaylord, *Basic Equations of Engineering Science*, McGraw-Hill, New York, 1964.
9. S. V. Patankar, *Numerical Heat Transfer and Fluid Flow*, McGraw-Hill, New York, 1980.
10. S. V. Patankar and D. B. Spalding, 'A calculation procedure for heat, mass and momentum transfer in three-dimensional parabolic flows', *Int. J. Heat Mass Transfer*, **15**, 1787–1806 (1972).
11. G. D. Raithby and G. E. Schneider, 'Numerical solution of problems in incompressible fluid flow: treatment of the velocity–pressure coupling', *Numer. Heat Transfer*, **2**, 417–440 (1979).
12. K. Velusamy, 'Introduction of whole field solution procedure and porous body formulations in THYC-2D', *Internal Note PFBR/66040/DN/1041/R-A*, IGCAR, 1989.
13. H. I. Rosten and D. B. Spalding, 'PHOENICS—beginners guide and user manual', *Rep. TR/100*, CHAM Ltd., 1986.
14. D. N. Roy, 'Laminar flow near the entry of coaxial tubes', *Appl. Sci. Res. A*, **14**, 421–430 (1965).
15. E. M. Sparrow and S. H. Lin, 'The developing laminar flow and pressure drop in entrance region of annular ducts', *J. Basic Eng.*, **86**, 827–834 (1964).
16. J. Liu, 'Flow of Bingham fluid in the entrance region of an annular tube', *M.S. Thesis*, University of Wisconsin, Milwaukee, WI, 1974.